



A Study on the Microstructure, Tensile and Fatigue Properties of Martensitic Stainless Steel Plate

Hyojoo Lee¹, Sam Yaw Anaman¹, Nam-Su Rho², Si-Hyun Sung², Hyun-Min Sung², Sang-Yeob Lee¹, and Hoon-Hwe Cho^{1,*}

¹Department of Materials Science and Engineering, Hanbat National University, Daejeon 34158, Republic of Korea.
²Production Engineering Research Institute, LG Electronics, Pyeongtaek 17709, Republic of Korea.

Abstract: The microstructure, tensile and fatigue properties of a martensitic stainless steel (MSS) plate with a thickness of 0.152 mm are investigated in this study. The microstructural properties were initially studied using electron backscatter diffraction microscopy. High dislocation densities were observed in the microstructure, along with the rolling texture revealed by the pole figure, following an initial cold rolling process of the as-received MSS plate. Tensile tests were conducted in both the rolling and transverse directions to compare the strength of the material in both directions. The results showed that the tensile strength was relatively low in the rolling direction. This can be attributed to the microstructure and crystallographic orientation of the material along that direction. Additional tensile tests were performed at various temperatures within the operating temperature range in the rolling direction. The results indicate that the highest tensile strength and elastic modulus are observed at room temperature. A high-cycle fatigue test was performed to determine the fatigue limit of the MSS plate. Furthermore, the microstructure was analyzed by controlling the fatigue cycles within the same stress range. The results revealed a proportional relationship between the accumulated deformation within the grains and the fatigue cycles. This can be helpful in understanding the fatigue damage mechanisms of the MSS plate.

(Received 30 June, 2023; Accepted 24 August, 2023)

Keywords: Martensitic Stainless Steel Plate, Microstructure, Tensile properties, Fatigue properties

1. INTRODUCTION

Martensitic stainless steel (MSS) is widely known and used in various industrial applications, such as steam generators, pressure vessels, mixer blades, cutting tools, and offshore platforms for oil extraction. This steel is commonly used to manufacture components for high- and low-temperature applications because of its excellent mechanical properties and reasonable corrosion resistance [1–3]. Among MSSs, American Iron and Steel Institute (AISI) 420 is a low-chromium MSS that is commercially available in low-carbon (carbon content less than 0.15%) and medium-carbon forms (maximum carbon content of 0.5%) [4,5].

The microstructures of AISI 420 MSS are typically

modified by various heat treatments for numerous industrial applications [6,7]. Generally, AISI 420 MSS exists commercially in an untampered state, which is extremely hard and brittle. The strength and wear resistance levels of AISI 420 MSS can be improved through tempering [4]. This steel is normally subjected to an initial hardening treatment prior to tempering. This treatment involves the transformation of the steel matrix into austenite at a specific temperature, followed by rapid quenching at a high cooling rate to obtain a complete martensitic structure [8,9]. Consequently, tempering is performed to relieve the residual stresses associated with the martensitic transformation to improve the toughness and formability of the steel [10,11]. This approach was reported by Tavares *et al.* [12], who indicated that steel tempering can be achieved at temperatures ranging from 200–700 °C. However, scholars generally do not recommend tempering in the range of 400–600 °C, as this process decreases impact toughness and corrosion resistance.

- 이효주: 석사과정, Sam Yaw Anaman: 박사 후 연구원, 노남수: 책임연구원, 성시현: 책임연구원, 성현민: 선임연구원, 이상엽: 부교수, 조훈휘: 부교수

*Corresponding Author: Hoon-Hwe Cho

[Tel: +82-42-821-1242, E-mail: hhcho@hanbat.ac.kr]

Copyright © The Korean Institute of Metals and Materials

Table 1. Chemical composition of the AISI 420 MSS used in this study (wt.%).

Element	C	Cr	Mn	Mo	P	Si	S	Fe
wt.%	0.38	13.5	0.55	1.0	≤ 0.025	0.40	≤ 0.010	Bal.

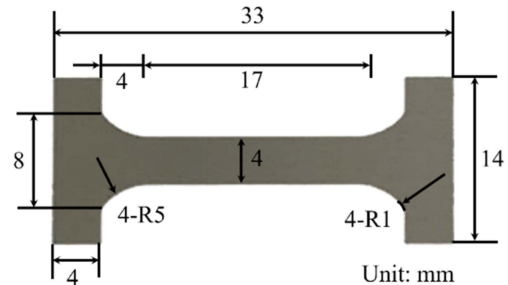
Furthermore, even though strength and toughness are important properties to consider when managing AISI 420 MSS, this steel is subjected to cyclic loading in most industrial applications. AISI 420 MSS experiences fracture due to repeated loading, predominantly under dynamic and cyclic loading conditions. This tendency to fracture leads to early fatigue failure and limits the widespread applicability of this steel [13]. Fatigue failure occurs in three stages: crack initiation, crack propagation, and ultimate fracture. The crack initiates with high shear stress at the surface and gradually propagates throughout the material once it reaches a certain crack growth length. Subsequently, permanent failure occurs during the final loading cycle [14]. Fatigue cracks usually occur on the surfaces of specimens, however, for high-cycle fatigue, cracks can initiate inside the material [15]. Reportedly, the fatigue failure of most metallic components depends significantly on the distribution of residual stress within the microstructure [16].

Overall, we aim to provide valuable insights into the variations in the microstructure of AISI 420 MSS plate with respect to its grain orientation and the influence of temperature on its mechanical strength. The mechanical properties at different temperatures along the rolling direction (RD) are investigated. Additionally, we aim to comprehensively study the fatigue properties of the plate and understand the mechanisms by which the degree of deformation resulting from the fatigue cycle affects its microstructure. The findings of this study can aid in improving the performance and reliability levels of MSS plates in various industrial applications.

2. EXPERIMENT

2.1. Chemical composition of the plate

Table 1 shows the chemical composition of the AISI 420 MSS used in this study. The MSS plate was processed by annealing treatment after cold rolling to the required thickness of 0.152 mm.

**Fig. 1.** Uniaxial tensile test specimen of the AISI MSS plate (dimensions in mm).

2.2 Evaluation of the microstructure and tensile properties

The microstructure of the AISI 420 MSS plate was observed using a field emission scanning electron microscope (FE-SEM; JSM-7100 F, JEOL, USA) equipped with an electron backscatter diffractometer (EBSD; TSL Hikari Super, TSL, USA). The plate was first mechanically polished and then chemically polished using colloidal silica until a mirror-like surface was achieved before the analysis. The orientation of each pixel was calculated from the measured Kikuchi diffraction patterns, and the patterns with average confidence index (CI) values of at least 0.8 were postprocessed using EBSD software (TSL OIM Analysis V8, TSL, USA).

To analyze the mechanical properties of the AISI 420 MSS plates, tensile tests were conducted using a high-temperature fatigue tester (MTS 810, MTS, USA) on a test specimen. The shape and dimensions of the tensile specimen are shown in Fig. 1, with a gauge length of 17 mm and a width of 4 mm. This specimen was tailored to accommodate the specific characteristics of the AISI MSS plate employed in this study, which possesses a slim thickness of 0.152 mm. Tensile specimens were initially sectioned out of the plate along the RD and transverse direction (TD). The temperature used during the tests was varied from room temperature to 200 °C, which is within the operating temperature range of the plate, to examine the effects of temperature on the tensile strength, yield strength, elastic modulus, and elongation of the

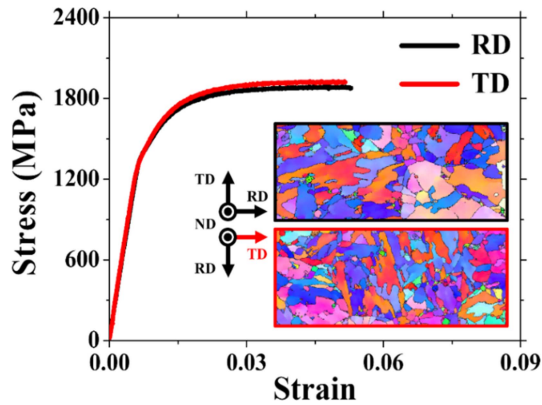


Fig. 4. Comparison of stress–strain curves: RD and TD of AISI 420 MSS plate.

Table 2. Tensile properties of RD and TD samples

Sample	Tensile strength (MPa)	Yield strength (MPa)	Elongation (%)
RD	1875.0 ± 26.8	1484.4 ± 10.9	5.3 ± 1.0
TD	1919.7 ± 18.1	1478.8 ± 7.5	5.1 ± 0.9

3(e)) showed that the plate developed a rolling texture due to cold rolling [18].

The room temperature tensile properties of the AISI 420 MSS plate in the RD and TD are presented in Fig. 4. The yield strength was determined by the 0.2% offset of the relatively low yield point on the curve, and the tensile strength was determined by the maximum point on the curve. The average values of the four tests based on the tensile test results are listed in Table 2. The tensile properties in the RD and TD showed slip-dominated flow. The yield point occurs at a high stress [19], and the yield strengths and elongation at fracture in both directions were almost similar; however, the tensile strength was slightly higher in the TD, by approximately 45 MPa. It is a well-known fact that texture can have a significant impact on tensile properties [20–22]. However, it can be observed that the tensile strength in the TD is higher than in the RD. This is attributed to the fact that the microstructure of the TD specimen has a greater abundance of grain boundaries due to its shorter grain axis length, compared to the RD specimen. Grain boundaries serve as barriers for the absorption or transmission of dislocations; this functions as a strengthening mechanism within the material [23–28]. Thus, it can be inferred that the mechanical properties are not heavily reliant on the

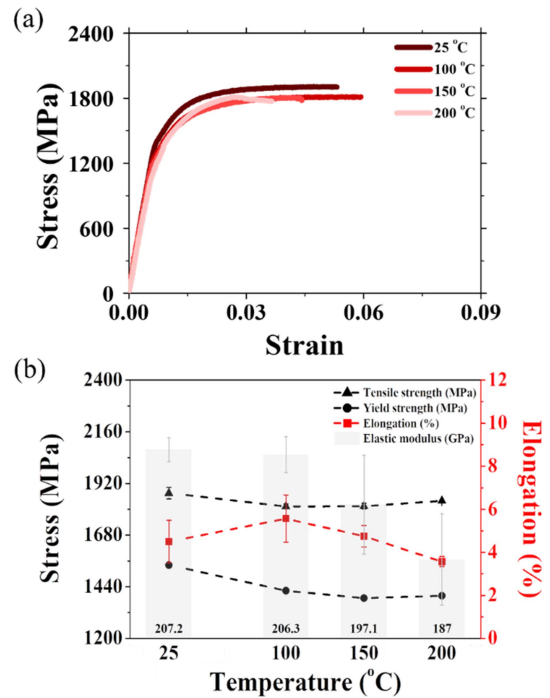


Fig. 5. (a) Stress–strain curve of the MSS plate at 25, 100, 150, and 200 °C, (b) Comparison of mechanical properties by temperature.

anisotropy of the texture. To further understand the mechanical properties of the plate, tensile tests at elevated temperatures (above room temperature) were conducted in the RD to investigate the temperature dependence of the mechanical properties of the MSS plate.

The variations in tensile properties with the temperatures of the specimens along the RD within the operating temperature range are shown in Fig. 5. Table 3 presents the average values of the results from three tests. The stress–strain curves based on the temperature are shown in Fig. 5(a). The variations in tensile properties, such as the yield strength, tensile strength, elastic modulus, and elongation with temperature, are shown in Fig. 5(b). The overall trend showed a decrease in the measured mechanical properties as the temperature increased. Both the tensile and yield strengths first decreased and then slightly increased with increasing temperature, while the elongation first increased and subsequently decreased. The temperature range where the tensile and yield strengths experienced a sudden increase was assumed to be associated with blue shortness. In carbon steel, it is common for the tensile strength to temporarily increase as the temperature increases due to blue shortness,

Table 3. Tensile properties of 25, 100, 150, and 200 °C samples.

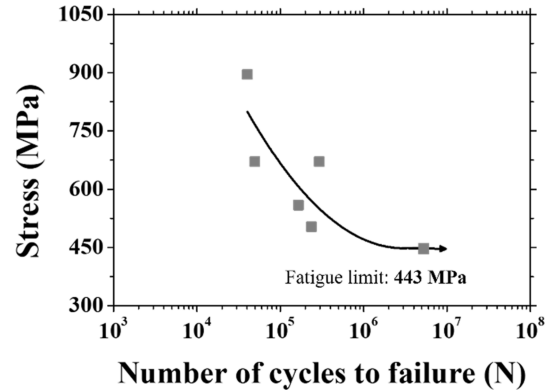
Temperature (°C)	Tensile strength (MPa)	Yield strength (MPa)	Elastic modulus (GPa)	Elongation (%)
25	1875.0 ± 26.8	1484.4 ± 10.9	207.2 ± 2.2	4.5 ± 1.0
100	1813.1 ± 11.1	1385.2 ± 4.6	206.3 ± 3.3	5.6 ± 1.1
150	1814.3 ± 13.0	1356.1 ± 7.4	197.1 ± 19.1	4.8 ± 0.5
200	1839.1 ± 1.4	1365.5 ± 10.9	187.0 ± 8.4	3.6 ± 0.2

peaking in a range of 200 °C–300 °C, before decreasing again [29,30]. This phenomenon could be caused by strain aging-strengthening of the material due to the precipitation of carbon or nitrogen when heated. According to reports, this effect should be more noticeable in steels with high carbon contents [30]. Similar to the findings of Zhao *et al.* [31], the relative increase in yield/tensile strength at 200 °C is estimated to be due to the effect of carbide precipitation from lath martensite. Lath martensite is formed by carbon atoms, which contribute to solid solution strengthening, and numerous dislocations generated by the martensitic transformation [31]. The decrease in elongation at 100 °C is attributed to the reduction in accumulated strain energy caused by the growth of grain boundaries and stress relaxation. When the temperature exceeded 150 °C, a significant decrease in elongation was observed, as shown in Fig. 5(b). This suggests the possibility of temper embrittlement due to the formation of more and coarser precipitates with increasing temperature [32,33].

3.2 Fatigue properties of the plate and deformation analysis according to cycle

The high cycle fatigue behavior of AISI 420 MSS plates was studied using stress-controlled fatigue tests, and the results are presented in a stress-life graph in Fig. 6. The stress life (S–N) curve predicted the fatigue life of AISI 420 MSS plates. It is portrayed on a log-log scale using the Basquin equation representing the relationship between stress amplitude and mean fatigue life in the finite life range [34]. From the results, the fatigue limit of the AISI 420 MSS plates was measured to be 447 MPa. Subsequently, a microstructure analysis of deformation with respect to fatigue cycles at different stress levels was conducted to better understand the results.

For high-cycle fatigue behavior, the mechanisms of crack initiation and propagation can vary depending on the

**Fig. 6.** S–N fatigue curves of specimens uniaxially fatigued at an R ratio of 0.1.

material. The number of cycles involved in crack initiation is a significant factor to consider when analyzing the fatigue life of a material [35]. In this part of the study, the origins of the differences in the high-cycle fatigue behavior were investigated. The specimens were tested by controlling the cycles at the intermediate stress and fatigue limits. Afterward, the microstructure of the surface of the AISI 420 MSS plate was observed using EBSD analysis. The EBSD results of a specimen with fatigue cycles, controlled at a stress of 671 MPa, are shown in Figs. 7(a–c), while the EBSD results of a failed specimen are shown in Fig. 7(d–f). The results indicate that the controlled specimen exhibited fewer LAGBs (19.1% (Fig. 7(b))) than the failed specimen (48.5%). Additionally, the average value measured from the KAM distribution was 0.43 (Fig. 7(c)) for the controlled specimen, which increased to 0.79 (Fig. 7(f)) in the failed specimen, indicating the accumulation of deformation within the grains in the failed specimen. Similarly, in the fatigue limit range, the EBSD results of the specimen with controlled fatigue cycles and the failed specimen are presented in Figs. 8(a–c) and Figs. 8(d–f), respectively. As observed at 671 MPa, the distributions and proportions of LAGBs increased with increasing number of cycles from 18.3% (Fig. 8(b)) to 23.2% (Fig. 8(e)). A

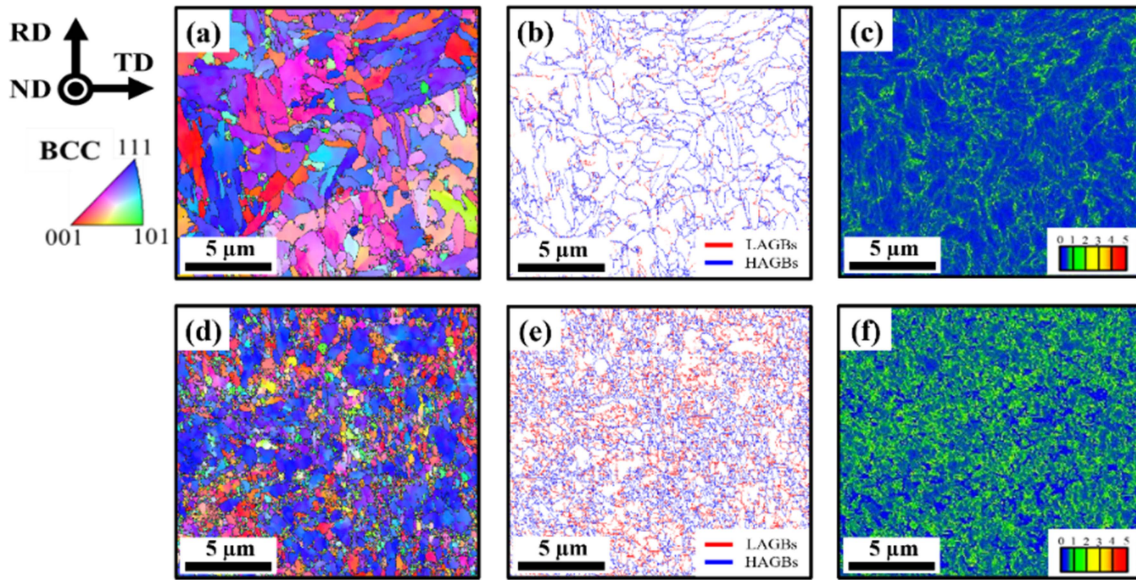


Fig. 7. ND-IPF, grain boundaries, and KAM maps for the specimen controlled for fatigue cycles (a–c) and the failed specimen (d–f) at 671 MPa.

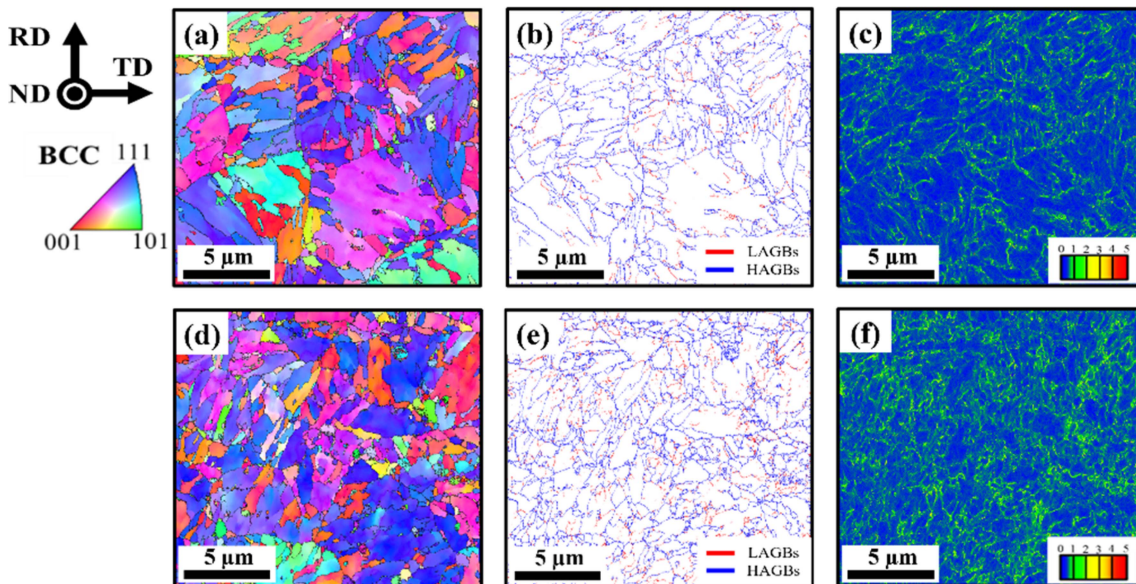


Fig. 8 ND-IPF, grain boundaries, and KAM maps for the specimen controlled for fatigue cycles (a–c) and the failed specimen (d–f) at the fatigue limit.

comparison of the average KAM values between Fig. 8(c) and Fig. 8(f) show that they increased from 0.40 to 0.50, indicating the accumulation of deformation within the grains. Because the stress level at the fatigue limit (447 MPa) was lower than at 671 MPa, fewer LAGBs and a lower KAM average value were observed. Consequently, it was observed that strain was built up within the grains and grain boundaries over the course of the fatigue cycle. This observation

confirmed that strain accumulation took place within the specimen as the fatigue cycle progressed. The heightened strain within these samples has the potential to initiate fatigue cracking [36–39].

5. CONCLUSIONS

In this study, the microstructural, tensile, and fatigue

properties of an AISI 420 MSS plate were analyzed. Afterward, the correlated effects of the microstructural changes on the fatigue properties of the plate were presented. The results were as follows:

1) The microstructure of the AISI 420 MSS plate underwent rolling deformation. The tensile tests performed along the rolling and transverse directions revealed that the mechanical properties along the rolling direction were inferior to those along the transverse direction, which can be inferred to mean that the mechanical properties are not heavily reliant on the anisotropy of the texture.

2) Tensile tests were performed at various temperatures within the operating temperature range along the RD. From the results, as the temperature increased, the overall tensile and yield strengths first decreased and then increased. Conversely, the elongation decreased with increasing temperature without exhibiting any increases. The phenomenon in which the strengths experienced an increase and a subsequent decrease potentially occurred due to blue shortness.

3) The fatigue limit of the plate was determined through high-cycle fatigue tests; based on the results, the difference in the amount of microstructural deformation was compared and analyzed by controlling the fatigue cycle. The amount of deformation was confirmed to accumulate inside the crystalline structure as the number of cycles increased.

ACKNOWLEDGEMENT

This study was supported by the National Research Foundation of Korea (NRF) grants funded by the Ministry of Science and ICT (MSIT) (No. NRF-2018R1A5A1025224). This work was supported by Institute for Information & communications Technology Promotion (IITP) grant funded by the Korea government (MSIP) (No.RS-2023-00222609). This research was supported by "Regional Innovation Strategy (RIS)" through the National Research Foundation of Korea (NRF) funded by the Ministry of Education (MOE) (2021RIS-004).

REFERENCES

1. A.N. Isfahany, H. Saghafian, G. Borhani, The effect of heat treatment on mechanical properties and corrosion behavior of AISI420 martensitic stainless steel, *J. Alloys Compd.* **509**, 3931–3936 (2011).
2. I. Alphonsa, A. Chainani, P.M. Raole, B. Ganguli, P.I. John, A study of martensitic stainless steel AISI 420 modified using plasma nitriding, *Surf. Coatings Technol.* **150**, 263–268 (2002).
3. K. Morshed-Behbahani, N. Zakerin, P. Najafisayar, M. Pakshir, A survey on the passivity of tempered AISI 420 martensitic stainless steel, *Corros. Sci.* **183**, 109340 (2021)
4. L.D. Barlow, M. Du Toit, Effect of austenitizing heat treatment on the microstructure and hardness of martensitic stainless steel AISI 420, *J. Mater. Eng. Perform.* **21**, 1327–1336 (2012).
5. G. Prieto, J.E.P. Ipiña, W.R. Tuckart, Cryogenic treatments on AISI 420 stainless steel: Microstructure and mechanical properties, *Mater. Sci. Eng. A.* **605**, 236–243 (2014).
6. B. Mahmoudi, M.J. Torkamany, A.R.S.R. Aghdam, J. Sabbaghzade, Laser surface hardening of AISI 420 stainless steel treated by pulsed Nd:YAG laser, *Mater. Des.* **31**, 2553–2560 (2010).
7. S. Dodds, A.H. Jones, S. Cater, Tribological enhancement of AISI 420 martensitic stainless steel through friction-stir processing, *Wear.* **302**, 863–877 (2013).
8. A. Rajasekhar, G. Madhusudhan Reddy, T. Mohandas, V.S.R. Murti, Influence of austenitizing temperature on microstructure and mechanical properties of AISI 431 martensitic stainless steel electron beam welds, *Mater. Des.* **30**, 1612–1624 (2009).
9. Y. Samih, G. Marcos, N. Stein, N. Allain, E. Fleury, C. Dong, T. Grosdidier, Microstructure modifications and associated hardness and corrosion improvements in the AISI 420 martensitic stainless steel treated by high current pulsed electron beam (HCPEB), *Surf. Coatings Technol.* **259**, 737–745 (2014).
10. K.H. Anantha, C. Örneke, S. Ejnermark, A. Medvedeva, J. Sjöström, J. Pan, Correlative Microstructure Analysis and In Situ Corrosion Study of AISI 420 Martensitic Stainless Steel for Plastic Molding Applications, *J. Electrochem. Soc.* **164** (2017) C85–C93.
11. S. Salahi, M. Kazemipour, A. Nasiri, Effects of microstructural evolution on the corrosion properties of AISI 420 martensitic stainless steel during cold rolling process, *Mater. Chem. Phys.* **258** (2021) 123916.
12. D. Fruchart, S. Miraglia, D. Laborie, Magnetic properties of an AISI 420 martensitic stainless steel, **312**, 307–314

- (2000).
13. R. Karimbaev, Y. Pyun, E. Maleki, O. Unal, A. Amanov, Materials Science & Engineering A An improvement in fatigue behavior of AISI 4340 steel by shot peening and ultrasonic nanocrystal surface modification, *Mater. Sci. Eng. A*. **791**, 139752 (2020).
 14. M. Ozturk, F. Husem, I. Karademir, E. Maleki, A. Amanov, O. Unal, Fatigue crack growth rate of AISI 4140 low alloy steel treated via shot peening and plasma nitriding, *Vacuum*. **207**, 111552 (2023).
 15. A. Umapathi, S. Swaroop, Measurement of residual stresses in titanium alloys using synchrotron radiation, *Meas. J. Int. Meas. Confed.* **140**, 518–525 (2019).
 16. C. Wang, K. Luo, X. Bu, Y. Su, J. Cai, Q. Zhang, J. Lu, Laser shock peening-induced surface gradient stress distribution and extension mechanism in corrosion fatigue life of AISI 420 stainless steel, *Corros. Sci.* **177**, 109027 (2020).
 17. ASTM E8, ASTM E8/E8M standard test methods for tension testing of metallic materials 1, *Annu. B. ASTM Stand.* **4**, 1–27 (2010).
 18. V.D. Sitdikov, R.K. Islamgaliev, G.F. Sitdikova, A. V. Ganeev, M.A. Nikitina, Unusual Rolling Texture in Ferritic/Martensitic Steel, *J. Mater. Eng. Perform.* **31**, 1971–1980 (2022).
 19. Z.P. Yu, Y.H. Yan, J. Yao, C. Wang, M. Zha, X.Y. Xu, Y. Liu, H.Y. Wang, Q.C. Jiang, Effect of tensile direction on mechanical properties and microstructural evolutions of rolled Mg-Al-Zn-Sn magnesium alloy sheets at room and elevated temperatures, *J. Alloys Compd.* **744**, 211–219 (2018).
 20. W.J. Kim, S.I. Hong, Y.S. Kim, S.H. Min, H.T. Jeong, J.D. Lee, Texture development and its effect on mechanical properties of an AZ61 Mg alloy fabricated by equal channel angular pressing, *Acta Mater.* **51**, 3293–3307 (2003).
 21. M. Rout, Texture-tensile properties correlation of 304 austenitic stainless steel rolled with the change in rolling direction Texture-tensile properties correlation of 304 austenitic stainless steel rolled with the change in rolling direction, *Mater. Res. Express.* **7**, 016563 (2020).
 22. S.H. Ryu, K. Il Kim, W. Noh, S.S. Kim, G.S. Cho, Effect of microstructural parameters on the tensile property of WC-12~22wt%Co cemented carbide, *J. Korean Inst. Met. Mater.* **59**, 201–208 (2021).
 23. Y.R. Ma, H.J. Yang, D.D. Ben, X.H. Shao, Y.Z.T.Q.W.Z.F. Zhang, Anisotropic Electroplastic Effects on the Mechanical Properties of a Nano - Lamellar Austenitic Stainless Steel, *Acta Metall. Sin* **34**, 534–542 (2021).
 24. I. Iordanova, V. Antonov, S. Gurkovsky, Changes of microstructure and mechanical properties of cold-rolled low carbon steel due to its surface treatment by Nd : glass pulsed laser, *Surf. Coatings Technol.* **153**, 267–275 (2002).
 25. M. Neslušán, M. Pitoňák, P. Minárik, M. Tkáč, P. Kollár, O. Životský, Influence of domain walls thickness, density and alignment on Barkhausen noise emission in low alloyed steels, *Sci. Rep.* **13**, 1–14 (2023).
 26. D.E. Spearot, M.D. Sangid, Insights on slip transmission at grain boundaries from atomistic simulations, *Curr. Opin. Solid State Mater. Sci.* **18**, 188–195 (2014).
 27. B. Yang, H. Vehoff, Dependence of nanohardness upon indentation size and grain size - A local examination of the interaction between dislocations and grain boundaries, *Acta Mater.* **55**, 849–856 (2007).
 28. J. Kacher, B.P. Eftink, B. Cui, I.M. Robertson, Dislocation interactions with grain boundaries, *Curr. Opin. Solid State Mater. Sci.* **18**, 227–243 (2014).
 29. I.-H. Hwang, A Development of SEM Applied Microjoining System, <https://www.e-jwj.org/upload/PDF/0/49/92/0499249.pdf> (2003).
 30. S. Trimethoxysilylmethyl, L. V Sherstyannikova, M.G. Voronkov, *E I E I E I*, **74**, 551–558 (2004).
 31. M.C. Zhao, T. Unenbayar, Y.C. Zhao, C. Liu, Y. Tian, D. Yin, A. Atrens, Influence of Tempering Temperature on the Microstructure and Mechanical Properties of a Cr-Ni-Mo-Alloyed Steel for Rock Drill Applications, *Steel Res. Int.* **90**, 1–5 (2019).
 32. I.A. Channa, A.A. Shah, S.H. Abro, M. Ali, Vol 2 No 1, *Sukkur IBA J. Emerg. Technol.* **2** (2019).
 33. C. Hwang, M. Joe, S. Kim, D. Han, K. Yoo, S. Kim, Y. Kim, S. Lee, J. Park, Evaluation and Prediction of Formation of Heat-Affected Zone and Mechanical Properties According to Welding Method of STS 316L/A516-70N Clad Plates, *J. Korean Inst. Met. Mater.* **60**, 873–883 (2022).
 34. S.H. Ryu, M.G. Jo, K. Il Kim, W. Noh, I.J. Hong, K.H. Lee, S.S. Kim, G.S. Cho, Tensile and Fatigue Characteristics of WC-20wt%Co Cemented Carbide with Sintering Methods, *J. Korean Inst. Met. Mater.* **60**, 227–236 (2022).
 35. S. Park, S. Kim, D. Lee, S. Ahn, S. Kim, Effect of microstructural factors on fatigue and fatigue crack propagation behaviors of mill-annealed Ti-6Al-4V alloy, *J. Korean Inst. Met. Mater.* **56**, 845–853 (2018).
 36. M.K. J. Polák, The dynamics of cyclic plastic deformation

- and fatigue life of low carbon steel at low temperatures, *Mater. Sci. Eng.* **26**, 157–166 (1976).
37. J. Man, T. Vystavěl, A. Weidner, I. Kuběna, M. Petrevec, T. Kruml, J. Polák, Study of cyclic strain localization and fatigue crack initiation using FIB technique, *Int. J. Fatigue*. **39**, 44–53 (2012).
38. O. Fatoba, R. Akid, Uniaxial cyclic elasto-plastic deformation and fatigue failure of API-5L X65 steel under various loading conditions, *Theor. Appl. Fract. Mech.* **94**, 147–159 (2018).
39. W. Gao, J. Lu, J. Zhou, L. Liu, J. Wang, Y. Zhang, Z. Zhang, Effect of grain size on deformation and fracture of Inconel718: An in-situ SEM-EBSD-DIC investigation, <https://www.sciencedirect.com/science/article/abs/pii/S0921509322017415?via%3Dihub> (2022).